2024 IEEE/RSJ International Conference on Intelligent Robots and Systems (IROS)
October 14-18, 2024. Abu Dhabi, UAE

High-Accuracy 2-D AoA Estimation Using Lightweight UWB Arrays

Yi Li[1], Hanying Zhao[1*], Yiman Liu[1], Tianyu Wang[3], Jincheng Yu[1],and Yuan Shen[1,2]

***Abstract*— Ultra-wide band (UWB) systems are gaining popularity for multi-robot localization benefiting from their high-accuracy ranging capabilities. However, current UWB systems fall short in determining orientations and realizing pair-wise localization for neglecting bearing information. Given the importance of bearing capabilities, especially when vision-based methods fail, this paper proposes a high-accuracy 2-D bearing estimation method using stereo UWB arrays. We propose a novel phase error calibration method that effectively mitigates various phase imperfections. This array is designed with antenna spacing larger than half the wavelength to diminish antenna coupling and enhance bearing accuracy. As regards the phase ambiguity issue arising from large antenna spacing, a distributed range-assisted phase ambiguity determination method is developed. Our bearing estimation method exhibits low complexity and is well-suited for the deployment on mobile robots with limited computational resources. The performance of the proposed method is validated on the practical platforms under dynamic scenarios, yielding root mean squared errors (RMSEs) less than 4° and 3° for azimuth and elevation angle estimation, respectively.**

I. Introduction

Cooperative multi-robot systems play an important role in a wide range of applications, notably in the Internet of Things (IoT) [1], intelligent transportation [2], as well as formation and control [3]. Ultra-wide band (UWB)-based localization systems have been increasingly applied in robot systems [3]–[5], featuring high accuracy, robustness to accumulated error, insensitivity to ambient light, and other advantages.

UWB localization systems typically rely on the fundamental principles of trilateration and triangulation, leveraging range and bearing measurements to determine position. Previous work have demonstrated the superior performance of ranging using UWB signals [6]–[8]. However, the exploration of UWB-based bearing estimation capabilities remains relatively limited and under-investigated. Bearing capability is crucial for robot networks owing to its pivotal role in providing pose perception capabilities, particularly when vision-based perception falls short. Recently, [9] proposed a range-based pose estimation approach that utilizes multiple UWB antennas mounted on robots. [10] investigated the influence of environmental scattering on electromagnetic signals and demonstrated an angle-of-arrival (AoA) estimation method using channel impulse response (CIR) measurements. The work in [11] introduced a pioneering framework for AoA estimation based on phase-difference-of-arrival (PDoA) measurements, in which a 2-element array is adopted using Decawave's DW1000 integrated circuit (IC). This approach leverages the higher resolution of PDoA measurements compared to range measurements, potentially leading to improved bearing estimation accuracy. However, in practice, various array imperfections, such as antennas mutual coupling and phase uncertainties, can significantly deteriorate the phase measurements of UWB signals, thus diminishing the bearing accuracy [12], [13].

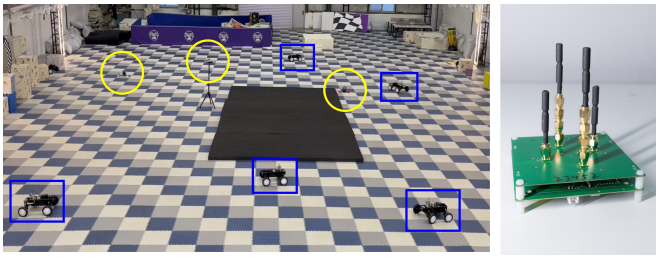

Fig. 1. The left hand side is our experiment environment, with unmanned vehicles (blue rectangular) and drones (yellow circle). The right hand side is our lightweight UWB arrays mounted on the unmanned vehicles and drones.

In this paper, we present a novel approach for 2-D AoA estimation in multi-robot systems operating in 3-D space, leveraging a stereo UWB array as depicted in Fig. 1. Our method addresses array imperfections through a comprehensive calibration process based on extensive experimental data. To mitigate the effects of mutual coupling, we increase the antenna spacing beyond half the wavelength, which introduces the challenge of phase ambiguity [14]. Therefore, we further propose a distributed range-assisted ambiguity resolution and 2-D AoA estimation algorithm, which leverages ranging results to correctly resolve the phase ambiguity. The effectiveness of our proposed method is validated through experiments conducted on our platforms, demonstrating remarkable accuracy with root mean squared error (RMSE) below 4° and 3° for azimuth and elevation angles, respectively.

II. Related Work

There have been various research studies on error models of antenna imperfections. Authors in [12] presented a data model for array-based AoA estimation, which considered the coupling effects, finite microwave switch isolation, and the phase center offset (PCO). However, only a narrowband system was considered, rendering the result unsuitable for UWB systems. In [15], the PCO of a UWB system was modeled and calibrated based on experimental data. Nevertheless, only

[1] The authors are with the Department of Electronic Engineering, and Beijing National Research Center for Information Science and Technology, Tsinghua University, Beijing 100084, China. (Hanying Zhao is the corresponding author*. E-mail: {li-yi20, liuyiman21}@mails.tsinghua.edu.cn, {hying_zhao, yu-jc, shenyuan_ee}@tsinghua.edu.cn).
[2] The author is with the Shanghai Artificial Intelligence Laboratory, Shanghai 200030, China.
[3] The author is with the QiYuan Lab, Beijing 100095, China (E-mail: wty17@tsinghua.org.cn).

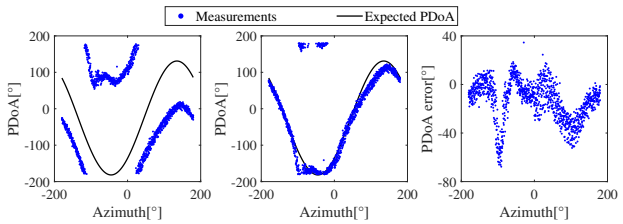

Fig. 2. (Left) The raw PDoA measurements with different AoAs. (Middle) The PDoA after calibrating the transmission delay. (Right) Except the transmission delay, there exist AoA-dependent PoA errors due to various imperfection factors.

a single antenna was equipped, and other imperfections such as mutual coupling effects among elements were overlooked. The work in [13] proposed a deep neural network-based method to address array imperfections, albeit without explicit phase-of-arrival (PoA) error modeling. However, its significant computation complexity hinders its deployment on devices with limited computational capabilities.

Apart from array imperfections, the PoA ambiguity issue also poses great challenge to AoA estimation. Typically, the PDoA measurements are inherently wrapped within the interval $[-\pi, \pi)$ even when the antenna spacing exceeds half a wavelength. Misresolution of PDoA ambiguity can lead to substantial errors in AoA estimation. To address this issue, a tracking method has been proposed to discern the ambiguous angles [16]. In [17], both time-difference-of-arrival (TDoA) and the PDoA measurements are utilized to facilitate the position estimation. More recently, [14] introduced a parallel soft positional information approach that encapsulates ambiguous positioning results. This method identifies valid ambiguities by searching for local maxima in the log-likelihood function. However, a limitation of these approaches is that they solely rely on single-link measurements, which may compromise stability in practical applications. Additionally, the angle searching procedures employed in these methods are computationally intensive, necessitating substantial computational resources.

III. Problem Formulation

Consider a multi-robot network with N nodes, and position of each node is $\boldsymbol{p}_i \in \mathbb{R}^3, i \in \mathcal{N} = \{1, 2, ..., N\}$. Each robot is equipped with an M-element array [1]. To improve the elevation resolution as well as eliminate the mutual coupling among antennas, we adopt a regular tetrahedron array with antenna spacing 0.622λ, where λ is the UWB signal wavelength. This design will incur the phase ambiguity issue since the antenna spacing exceeds half the signal wavelength.

In the local coordinate system of node i, the position of the m-th antenna within the array is denoted as $\boldsymbol{q}_m, m \in \mathcal{M} = \{1, 2, ..., M\}$. Without loss of generality, we designate antenna 1 as the reference point and set its position as $\boldsymbol{q}_1 = \mathbf{0}$. Given an incident signal arriving from a direction specified

[1]In this paper, we assume that the array configurations of all nodes are uniform. Nonetheless, our method remains applicable to arrays featuring diverse geometrical configurations.

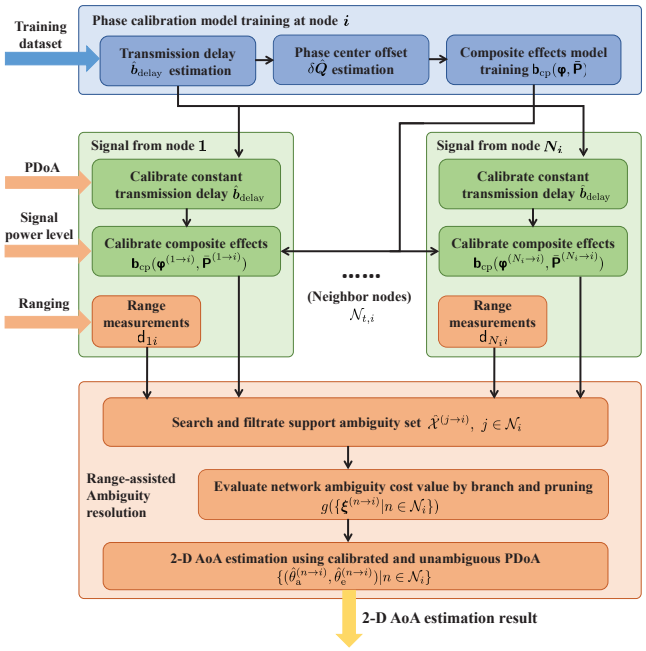

Fig. 3. The comprehensive flowchart of the proposed 2-D AoA estimation method, including the phase calibration model training (blue blocks), the phase calibration procedure (greed blocks), the ambiguity resolution process and the AoA estimation using processed PDoA (orange blocks).

by $\boldsymbol{\theta} = [\theta_{\text{a}}, \theta_{\text{e}}]^{\text{T}}$, where θ_{a} represents the azimuth AoA and θ_{e} represents the elevation AoA, the PDoA between antennas m and 1 is given by

$$\varphi_m = \boldsymbol{q}_m^{\text{T}} \boldsymbol{k}(\boldsymbol{\theta}) + \mathsf{e}_m - 2\xi_m \pi, \tag{1}$$

where $\boldsymbol{k}(\boldsymbol{\theta}) = 2\pi/\lambda \left[\cos\theta_{\text{e}} \cos\theta_{\text{a}}, \cos\theta_{\text{e}} \sin\theta_{\text{a}}, \sin\theta_{\text{e}}\right]^{\text{T}}$ is the wave vector, e_m is the phase error, and $\xi_m \in \mathbb{Z}$ denotes the unknown ambiguity.

In this paper, we aim to achieve high-accuracy estimation of AoA $\boldsymbol{\theta}$ from noisy PDoA measurements $\boldsymbol{\varphi} = [\varphi_2 \ \varphi_3 \ \cdots \ \varphi_M]^{\text{T}}$. There are two challenges, i.e., array imperfections and phase ambiguity issues. Indeed, the assumption that the phase error e_m can be modeled as additive white Gaussian noise (AWGN) is often an oversimplification. In reality, the phase error can arise from a multitude of factors, which significantly impacts the accuracy of AoA estimation. On the other hand, when the antenna spacing exceeds half the wavelength, the phase ambiguity issue may arise. Resolving the ambiguity accurately is crucial for obtaining high-accuracy AoA estimation.

IV. 2-D AoA Estimation

In this section, first, the phase error model is thoroughly examined, and a corresponding calibration method is introduced to mitigate its effects. Furthermore, we presents a novel distributed range-assisted ambiguity determination approach, which resolves the phase ambiguity with low-complexity. The comprehensive flowchart of the proposed 2-D AoA estimation algorithm is illustrated in Fig. 3.

A. Phase Error Model

Drawing upon previous research [12], [13], [15], [18], as well as empirical data collected on our UWB platform, we formulate the following phase error model

$$\mathsf{e}_m = b_{\mathrm{delay},m} + \delta \boldsymbol{q}_m^{\mathrm{T}} \boldsymbol{k}(\boldsymbol{\theta}) + b_{\mathrm{PCV},m}(\boldsymbol{\theta}) + \mathsf{b}_{\mathrm{others},m} + \mathsf{w}_m, \tag{2}$$

which encapsulates the transmission delay, the phase center deviation, mutual coupling effects, thermal noise and other unknown imperfections. First, the **transmission delay** $b_{\mathrm{delay},m}$ arises from different lengths of transmission lines, which is constant. Second, the **phase center deviation** is considered, which arises due to the deviation of the apparent source of radiation from the geometrical center of the antenna [18]. Moreover, it is partitioned into two components, the invariant part, i.e., the PCO $\delta \boldsymbol{q}_m$, and the AoA-dependent part, i.e., the phase center variations (PCV) $b_{\mathrm{PCV},m}(\boldsymbol{\theta})$. Third, the other effects, including the **mutual coupling effects**, **phase uncertainties** and other unknown imperfections, are encompassed into $\mathsf{b}_{\mathrm{others},m}$. Finally, $\mathsf{w}_m \sim \mathcal{N}(0, \sigma_{\mathrm{n}}^2)$ represents the stochastic **thermal noise**. Recognizing the challenge in analytically modeling all these factors, we reformulate the PDoA error model as follows[2]

$$\mathsf{b}_{\mathrm{cp},m}(\boldsymbol{\varphi}, \bar{\mathbf{P}}) := b_{\mathrm{PCV},m}(\boldsymbol{\theta}) + \mathsf{b}_{\mathrm{others},m}, \tag{3}$$

where $\mathsf{b}_{\mathrm{cp},m}$ encompasses the PCV item, mutual coupling effects and other unknown imperfect factors. Here, $\bar{\mathbf{P}} = \mathbf{P}/(\Pi_{m=1}^{M} \mathbf{P}_m)^{1/M}$ represents the normalized received signal power level across all antennas, calculated as the received power divided by the geometric mean of the power levels. To mitigate computational complexity, full CIR samples are not utilized in this model, while they may provide more comprehensive information.

B. Phase Calibration Method

In the following, we present a calibration methodology tailored to address the various imperfection factors outlined in Eq. (2) and Eq. (3).

Phase model training: For a particular array, there is the training dataset $\mathcal{D} = \{(\boldsymbol{\theta}^{(i)}, \boldsymbol{\varphi}^{(i)}, \mathbf{P}^{(i)}), i = 1, 2, ..., D\}$. Both the PDoA $\boldsymbol{\varphi}^{(i)}$ and the received signal power $\mathbf{P}^{(i)}$ are extracted from the CIR, specifically by employing the leading edge detection algorithm [11].

First, the transmission delay is estimated by

$$\hat{b}_{\mathrm{delay},m} = \mathbb{E}_{\theta_{\mathrm{a}}|\theta_{\mathrm{e}}=0} \left[\varphi_m - \boldsymbol{q}_m^{\mathrm{T}} \boldsymbol{k}(\boldsymbol{\theta}) \right]. \tag{4}$$

The expectation $\mathbb{E}_{\theta_{\mathrm{a}}|\theta_{\mathrm{e}}=0}[\cdot]$ is approximated by the empirical average on the horizontal plane.

Next, we estimate the PCO by least-square (LS) method

$$\delta \hat{\boldsymbol{q}}_m = \arg \min_{\boldsymbol{x} \in \mathbb{R}^3} \sum_{i=1}^{D} \left\| \varphi_m^{(i)} - \hat{b}_{\mathrm{delay},m} - (\boldsymbol{q}_m + \boldsymbol{x})^{\mathrm{T}} \boldsymbol{k}(\boldsymbol{\theta}^{(i)}) \right\|^2,$$

and the closed-form solution is given by

$$\delta \hat{\boldsymbol{q}}_m = (\boldsymbol{K}\boldsymbol{K}^{\mathrm{T}})^{-1} \boldsymbol{K} (\boldsymbol{\phi}_m - \hat{b}_{\mathrm{delay},m}) - \boldsymbol{q}_m, \tag{5}$$

[2]During phase calibration, the phase ambiguity is unknown and the wrapped PDoA is adopted.

where $\boldsymbol{K} = [\boldsymbol{k}(\boldsymbol{\theta}^{(1)}) \ \boldsymbol{k}(\boldsymbol{\theta}^{(2)}) \ \cdots \ \boldsymbol{k}(\boldsymbol{\theta}^{(D)})]$ and $\boldsymbol{\phi}_m$ is the stacking vector of $\varphi_m^{(i)}$.

Third, the residual phase error, $\mathsf{b}_{\mathrm{cp},m} + \mathsf{w}_m$, is modeled using Gaussian process (GP) theory. For brevity, let $\mathsf{y}_m^{(i)} := \mathsf{b}_{\mathrm{cp},m}^{(i)} + \mathsf{w}_m^{(i)}$, and $\mathbf{x}^{(i)} := [\boldsymbol{\varphi}^{(i)\mathrm{T}} \ \bar{\mathbf{P}}^{(i)\mathrm{T}}]^{\mathrm{T}}$ denote the composite residual error and the input feature vector, respectively. We impose GP priors on the composite phase bias $\mathsf{b}_{\mathrm{cp},m}$, with the distributions given by

$$p(\mathbf{b}_{\mathrm{cp},m}) = \mathcal{N}(\mathbf{0}, \boldsymbol{R}_m) \ \text{ and } \ p(\mathbf{y}_m) = \mathcal{N}(\mathbf{0}, \boldsymbol{R}_m + \sigma_{\mathrm{n}}^2 \boldsymbol{I}),$$

where $\mathbf{y}_m$ and $\mathbf{b}_{\mathrm{cp},m}$ are the concatenated vectors of $\mathsf{y}_m^{(i)}$ and $\mathsf{b}_{\mathrm{cp},m}^{(i)}$ across all training samples. The covariance matrix $\boldsymbol{R}_m$ is constructed using a squared exponential kernel function $\omega(\mathbf{x}^{(i)}, \mathbf{x}^{(j)})$ with hyperparameters $\boldsymbol{\Sigma}$.

Given the computational challenges of the full GP method for large training datasets, we employ the sparse GP approach as described in [19]. This approach introduces a small set of inducing variables $\mathbf{b}'_{\mathrm{cp},m}$ evaluated at the pseudo-inputs $\mathbf{X}'$, which are independent from the training data $\mathbf{X} = [\mathbf{x}^{(1)} \ \mathbf{x}^{(2)} \ \cdots \ \mathbf{x}^{(D)}]$. Define a variational distribution $q(\mathbf{b}'_{\mathrm{cp},m}) = \mathcal{N}(\boldsymbol{\mu}_m, \boldsymbol{U}_m)$, and the evidence lower bound (ELBO) of the log marginal likelihood is given by

$$\begin{aligned} \mathcal{L}_m(\mathbf{X}', \sigma_{\mathrm{n}}^2, \boldsymbol{\Sigma}) = \log \mathcal{N}(\mathbf{y}_m | \mathbf{0}, \sigma_{\mathrm{n}}^2 \boldsymbol{I} + \hbar(\mathbf{X}, \mathbf{X})) \\ - \frac{1}{2\sigma_{\mathrm{n}}^2} \operatorname{tr} \left(\omega(\mathbf{X}, \mathbf{X}) - \hbar(\mathbf{X}, \mathbf{X}) \right), \end{aligned} \tag{6}$$

where $\hbar(\mathbf{X}, \mathbf{X}) = \omega(\mathbf{X}, \mathbf{X}')\omega(\mathbf{X}', \mathbf{X}')^{-1}\omega(\mathbf{X}', \mathbf{X})$. During the training phase, the ELBO in Eq. (6) is optimized over pseudo-inputs $\mathbf{X}'$ and hyperparameters $\sigma_{\mathrm{n}}^2, \boldsymbol{\Sigma}$ by numerical methods. Following the guidelines in [19], the optimal variational parameters $\boldsymbol{\mu}_m^*$ and $\boldsymbol{U}_m^*$ can be derived.

Phase calibration: Once the transmission delay $\hat{b}_{\mathrm{delay},m}$, the PCO $\delta \hat{\boldsymbol{q}}_m$, and the GP parameters $\sigma_p^2, \boldsymbol{\Sigma}, \boldsymbol{\mu}_m^*, \boldsymbol{U}_m^*$ have been obtained, the PDoA can be calibrated for new inputs $\mathbf{x} = [\boldsymbol{\varphi}^{\mathrm{T}} \ \bar{\mathbf{P}}^{\mathrm{T}}]^{\mathrm{T}}$ as follows

$$\hat{\varphi}_m = \varphi_m - \hat{b}_{\mathrm{delay},m} - \hat{\mathsf{b}}_{\mathrm{cp},m}, \tag{7}$$

where $\hat{\mathsf{b}}_{\mathrm{cp},m}$ is characterized by $p(\hat{\mathsf{b}}_{\mathrm{cp},m}) = \mathcal{N}(\hat{\mu}, \hat{\sigma}^2)$, with

$$\begin{aligned} \hat{\mu} &= \omega(\mathbf{x}, \mathbf{X}')\omega(\mathbf{X}', \mathbf{X}')^{-1} \boldsymbol{\mu}_m^*, \\ \hat{\sigma}^2 &= \omega(\mathbf{x}, \mathbf{x}) - \omega(\mathbf{x}, \mathbf{X}')\omega(\mathbf{X}', \mathbf{X}')^{-1}\omega(\mathbf{X}', \mathbf{x}) \\ &\quad + \omega(\mathbf{x}, \mathbf{X}')\omega(\mathbf{X}', \mathbf{X}')^{-1} \boldsymbol{U}_m^* \omega(\mathbf{X}', \mathbf{X}')^{-1}\omega(\mathbf{X}', \mathbf{x}). \end{aligned}$$

After completing all the aforementioned calibrations, the processed PDoA for M elements can be expressed as

$$\hat{\boldsymbol{\varphi}} = \hat{\boldsymbol{Q}}^{\mathrm{T}} \boldsymbol{k}(\boldsymbol{\theta}) - 2\pi \boldsymbol{\xi} + \boldsymbol{\nu}, \tag{8}$$

where $\hat{\boldsymbol{Q}} = [\hat{\boldsymbol{q}}_2 \ \hat{\boldsymbol{q}}_3 \ \cdots \ \hat{\boldsymbol{q}}_M]$, and $\hat{\boldsymbol{q}}_m = \boldsymbol{q}_m + \delta \hat{\boldsymbol{q}}_m$ are the calibrated element positions, and the residual noise $\boldsymbol{\nu}$ is assumed to follow a Gaussian distribution $\boldsymbol{\nu} \sim \mathcal{N}(\mathbf{0}, \sigma_{\mathrm{n}}^2 \boldsymbol{I})$. In the following, the calibrated phase will be leveraged to resolve the ambiguities $\boldsymbol{\xi}$ and to estimate the AoA.

C. Ambiguity Resolution

As regards the ambiguity resolution, the phase ambiguities $\xi_m \in \mathbb{Z}$ in Eq. (1) are supposed to be determined. Before delving into our proposed method, it is essential to establish the range measurements model. Consider a network consisting of N nodes, indexed by $\mathcal{N} = \{1, 2, 3, \ldots, N\}$. For any node i, its neighbor nodes are denoted by $\mathcal{N}_i$. When a signal is transmitted by node j and received at node i, the PDoA is denoted as $\hat{\boldsymbol{\varphi}}^{(j\to i)}$. Additionally, the range measurement between nodes i and j is given by

$$\mathsf{d}_{ij} = \|\boldsymbol{p}_i - \boldsymbol{p}_j\| + \mathsf{u}_{ij}, \tag{9}$$

where $\mathsf{u}_{ij} \sim \mathcal{N}(0, \sigma_{\mathrm{d}}^2)$ represents the ranging noise. In the following, our objective is to determine the unknown ambiguities $\{\boldsymbol{\xi}^{(j\to i)} = [\xi_2^{(j\to i)} \ \xi_3^{(j\to i)} \ \cdots \ \xi_M^{(j\to i)}]^{\mathrm{T}}, i, j \in \mathcal{N}\}$ from the PDoA and network range measurements.

By leveraging the network range measurements, we exclude unreasonable ambiguities according to geometry relationships among nodes, thereby reducing the ambiguity. Specifically, for node i, given PDoA and network range measurements, we define a network ambiguity cost function as follows

$$g(\{\boldsymbol{\xi}^{(n\to i)} | n \in \mathcal{N}_i\}) = \sum_{j,k\in\mathcal{N}_i} e(\boldsymbol{\xi}^{(j\to i)}, \boldsymbol{\xi}^{(k\to i)}), \tag{10}$$

in which $e(\boldsymbol{\xi}^{(j\to i)}, \boldsymbol{\xi}^{(k\to i)})$ is the cost value associated with the pair of edges (j, i) and (k, i), defined by

$$e(\boldsymbol{\xi}^{(j\to i)}, \boldsymbol{\xi}^{(k\to i)}) = \left| \boldsymbol{\kappa}(\boldsymbol{\xi}^{(j\to i)})^{\mathrm{T}} \boldsymbol{\kappa}(\boldsymbol{\xi}^{(k\to i)}) - \frac{\mathsf{d}_{ij}^2 + \mathsf{d}_{ik}^2 - \mathsf{d}_{jk}^2}{2\mathsf{d}_{ij}\mathsf{d}_{ik}} \right|. \tag{11}$$

In Eq. (11), $\boldsymbol{\kappa}(\boldsymbol{\xi}^{(j\to i)})$ is the estimated wave vector, accompanied with PDoA measurements $\hat{\boldsymbol{\varphi}}^{(j\to i)}$, given by

$$\boldsymbol{\kappa}(\boldsymbol{\xi}^{(j\to i)}) = \hat{\boldsymbol{Q}}^{\mathrm{T}\dagger}(\hat{\boldsymbol{\varphi}}^{(j\to i)} + 2\pi\boldsymbol{\xi}^{(j\to i)}), \tag{12}$$

where $(\cdot)^\dagger$ denoted the Moore-Penrose inverse of the input matrix. For the true ambiguity $\boldsymbol{\xi}_*^{(j\to i)}$, the corresponding estimated wave vector $\boldsymbol{\kappa}(\boldsymbol{\xi}_*^{(j\to i)})$ will closely approximate the true wave vector, i.e., $\boldsymbol{\kappa}(\boldsymbol{\xi}_*^{(j\to i)}) \approx \boldsymbol{k}(\boldsymbol{\theta}^{(j\to i)})$. Therefore we have that $e(\cdot)$ approaches 0 at the true ambiguity, and yields large positive value at other wrong ambiguities. This behavior facilitates the ambiguity resolution. Furthermore, by incorporating all possible binary combinations of neighbor nodes $n \in \mathcal{N}_i$ into the network ambiguity cost function $g(\cdot)$ in Eq. (10), we enhance the robustness of the method through cross-validation.

Based on the proposed network ambiguity cost function, the ambiguity at node i can be determined by

$$\min_{\boldsymbol{\xi}} g(\{\boldsymbol{\xi}^{(n\to i)} | n \in \mathcal{N}_i\}), \tag{13}$$

in which the joint ambiguity set $\{\boldsymbol{\xi}^{(n\to i)} | n \in \mathcal{N}_i\}$ is optimized. However, it is an NP-hard combinatorial optimization problem. Consequently, a branch-and-prune method is adopted to determine the ambiguity at each node locally, with low computational complexity. Specifically, we first search the candidate set of phase ambiguity of all nodes. Then, take each node in the network sequentially and traverse all the ambiguity combinations. After evaluating the proposed network ambiguity cost function (10), the candidates associated with too large cost value are pruned to reduce the computation complexity. Finally, the output ambiguity is given by the one with the minimal ambiguity cost.

Given the determined phase ambiguity $\{\hat{\boldsymbol{\xi}}_*^{(j\to i)}, j \in \mathcal{N}_i\}$, the 2-D AoA is estimated by

$$\hat{\boldsymbol{\kappa}}(\hat{\boldsymbol{\xi}}_*^{(j\to i)}) = \hat{\boldsymbol{Q}}^{\mathrm{T}\dagger}(\hat{\boldsymbol{\varphi}}^{(j\to i)} + 2\pi\hat{\boldsymbol{\xi}}_*^{(j\to i)}), \tag{14a}$$

$$\hat{\theta}_{\mathrm{a}}^{(j\to i)} = \arctan([\hat{\boldsymbol{\kappa}}]_2/[\hat{\boldsymbol{\kappa}}]_1), \tag{14b}$$

$$\hat{\theta}_{\mathrm{e}}^{(j\to i)} = \arctan([\hat{\boldsymbol{\kappa}}]_3/\|[\hat{\boldsymbol{\kappa}}]_{1:2}\|). \tag{14c}$$

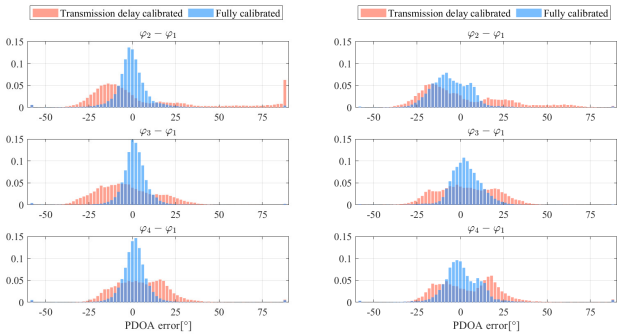

(a) (b)

Fig. 4. Post-calibration histogram of PDoA error: (a) calibration with dedicated trained models for each of 5 arrays; (b) unified calibration using solely the trained model of array 1 for all remaining arrays.

V. Experiments

To evaluate the performance of the proposed 2-D AoA estimation method, several experiments are conducted on our 4-element UWB platforms, as shown in Fig. 1. Each antenna is equipped with a Decawave's DW1000 transceiver, and the channel 2 with carrier frequency 3993.6MHz is used. Antenna spacing of the regular tetrahedron array is 46.67mm, larger than the half-wavelength 37.5mm.

As shown in Fig. 1, eight arrays were mounted on free moving unmanned vehicles and drones, simultaneously collecting PDoA measurements. Data on three drones were not collected due to the limited space. The motion capture system used is the *FZMotion Mocap System* [20], which provides millimeter-level positioning accuracy and serves as the groundtruth. The experiments were conducted three times, each lasting about 200 seconds and generating a dataset of roughly 6500 entries per iteration.

A. Phase calibration

To verify the effectiveness of the proposed phase calibration method, two of the three iterations were used for training and the other one was used for test. In current practice, only the transmission delay is typically considered and calibrated in UWB systems. Therefore, the baseline method is set

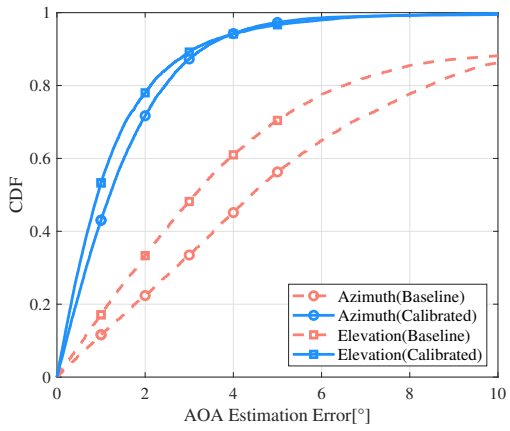

Fig. 5. The CDF of azimuth and elevation estimation error of the baseline and fully calibrated phase. The AoA estimation performance is improved drastically benefiting from the favourable phase calibration.

TABLE I
THE RMSE[°] OF PDOA CALIBRATION.

Array ID	1	2	3	4	5
Delay calibrated	23.6	24.3	24.7	20.3	18.4
Fully calibrated with dedicated trained models	10.0	9.1	11.2	6.2	6.8
Calibrated with a mismatched model	/	17.2	13.5	9.8	10.6

by only calibrating the delay item, i.e. b_{delay} in Eq. (2). However, despite calibrating the transmission delay, a time-varying (specifically, AoA-dependent) phase bias persists, leading to significant deviations. For all five arrays, the post-calibration histograms of the PDoA error are illustrated in Fig. 4(a). Utilizing the proposed phase error model and calibration method outlined in Section IV, the PDoA error is reduced to closely resemble AWGN noise with a small variance. And the RMSE of PDoA after different calibration methods are given in Table I.

Based on the calibrated PDoAs, the 2-D AoA estimation RMSEs of five arrays are presented in Table II. The cumulative distribution function (CDF) plot of AoA estimation error is given in Fig. 5. In the baseline method, the probability of estimation error exceeding 10° is higher than 10% when only transmission delay is calibrated. After the full calibration, the large phase bias is eliminated and both the azimuth and elevation estimation errors decrease to within 5° with a probability greater than 95%.

To evaluate the generalization ability of the proposed phase calibration method on different arrays, the phase error

TABLE II
THE RMSE[°] OF AOA ESTIMATION.

Array ID	1	2	3	4	5
Azimuth	3.8	1.7	2.7	1.9	1.9
Elevation	3.0	1.3	2.3	1.7	1.3

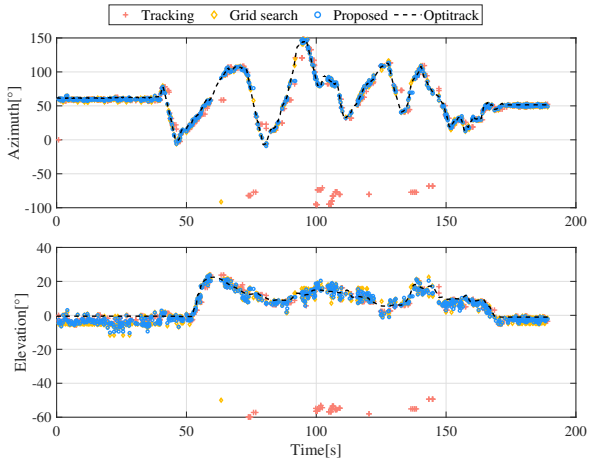

Fig. 6. The AoA estimation result of one edge in one experiment. There are occasions that either the AoA tracking method or the grid search method is misled to the wrong ambiguity, and thus large AoA estimation error appears.

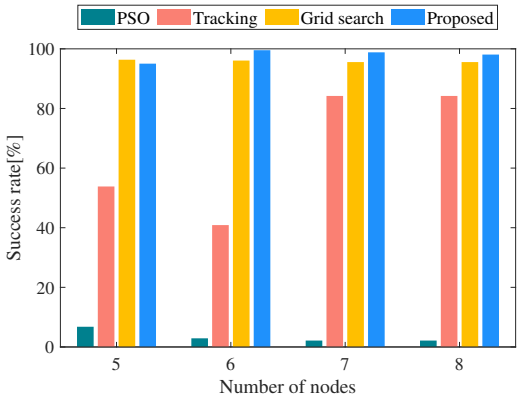

Fig. 7. Probability of successfully resolving the ambiguity. The proposed method achieves high success rate and exhibits stable performance.

model specifically trained for array 1 is used to calibrate the other four arrays, and histograms of the PDoA error are shown in Fig. 4(b). Moreover, Table I details the RMSEs of the calibrated PDoA for the arrays. Notably, there are still pronounced reductions in the PDoA error, indicating the method's generalization ability. However, it is also observed that the calibration performance slightly diminishes in the test arrays compared to the trained array

B. Ambiguity resolution

After phase calibration, the refined PDoAs are then utilized for ambiguity resolution and AoA estimation. The proposed method is compared with several established algorithms, the particle swarm optimization (PSO) method [17], the AoA tracking method [16], and the grid search method [14]. Four experiments were conducted, and the number of nodes was 5,6,7, and 8, respectively.

Fig. 6 showcases AoA estimation results of a specific link in a experiment trial. The PSO method is not illustrated since it fails to resolve the ambiguity almost all the time.

TABLE III
THE COMPUTATIONAL COMPLEXITY.

Computation time[ms]	5 nodes	6 nodes	7 nodes	8 nodes
PSO [17]	1095.6	1389.5	1424.6	1569.5
Tracking [16]	47.2	60.6	75.1	94.3
Grid search [14]	774.8	976.2	1127.4	1317.9
Proposed	**0.263**	**0.315**	**0.281**	**0.301**

According to Fig. 6, there are instances that both the AoA tracking method and the grid search method converge on the wrong ambiguity. In contrast, the proposed method consistently identifies the correct ambiguity. To quantify the performance of various methods in resolving ambiguities, we analyzed the worst-case scenario across all links within each experiment. The resulting success rates are presented in Fig. 7. The PSO method demonstrates an exceedingly low success rate, primarily attributed to its heavy reliance on accurate position estimations. The tracking method, on the other hand, exhibits instability, with its success rate fluctuating significantly between experiments. This is because it depends on the ambiguity resolution result at the beginning, and erroneous angle estimates propagate throughout the estimation process if an ambiguous angle is encountered initially. Both the grid search method and the proposed method achieve high success rates across all experiments. However, when it comes to computational complexity, the proposed method shines. The average computation time per instance processed at each node is detailed in Table III. Notably, the proposed method significantly outperforms the other approaches, requiring substantially less time and thus being suited for lightweight robots constrained by limited computational resources.

VI. CONCLUSION

This paper presents a high-accuracy 2-D AoA estimation method employing lightweight UWB arrays. First, we adopted a 4-element stereo array with antenna spacing exceeding half the wavelength, aimed at enhancing the elevation resolution and mitigating the antenna mutual coupling. Second, we devised a novel phase calibration methodology that effectively eliminates PDoA measurement errors incurred by the transmission delay, antenna phase center deviation and mutual coupling effects. To further address the ambiguity issue arising from large antenna spacings, we proposed an online AoA estimation algorithm along with a distributed ambiguity resolution method, where range measurements are leveraged to enhance the ambiguity resolution. The proposed method exhibits low computational overhead and is well-suited for mobile robots. Real-world experiments were conducted, which attains RMSEs less than 4° and 3° for azimuth and elevation estimation, respectively.

VII. ACKNOWLEDGMENT

This work was supported in part by the National Natural Science Foundation of China under Grant 62271285, in part by the National Natural Science Foundation of China under Grant 62203257, in part by Tsinghua University-Meituan Joint Institute for Digital Life, and in part by Shanghai AI Laboratory.

REFERENCES

[1] Y. Rizk, M. Awad, and E. W. Tunstel, "Cooperative heterogeneous multi-robot systems: A survey," *ACM Comput. Surv.*, vol. 52, no. 2, apr 2019. [Online]. Available: https://doi.org/10.1145/3303848

[2] Y. Tian, Y. Chang, F. Herrera Arias, C. Nieto-Granda, J. P. How, and L. Carlone, "Kimera-multi: Robust, distributed, dense metric-semantic slam for multi-robot systems," *IEEE Trans. Robot.*, vol. 38, no. 4, pp. 2022–2038, 2022.

[3] X. Zhou, X. Wen, Z. Wang, Y. Gao, H. Li, Q. Wang, T. Yang, H. Lu, Y. Cao, C. Xu, and F. Gao, "Swarm of micro flying robots in the wild," *Science Robotics*, vol. 7, no. 66, p. eabm5954, 2022. [Online]. Available: https://www.science.org/doi/abs/10.1126/scirobotics.abm5954

[4] B. Yang, J. Li, and H. Zhang, "Uvip: Robust uwb aided visual-inertial positioning system for complex indoor environments," in *Proc. IEEE Int. Conf. Robot. Autom.*, 2021, pp. 5454–5460.

[5] H. A. G. C. Premachandra, R. Liu, C. Yuen, and U.-X. Tan, "Uwb radar slam: An anchorless approach in vision denied indoor environments," *IEEE Robot. Autom. Lett.*, vol. 8, no. 9, pp. 5299–5306, 2023.

[6] D. Neirynck, E. Luk, and M. McLaughlin, "An alternative double-sided two-way ranging method," in *Proc. Workshop Pos., Nav. Commun.*, Bremen, Germany, Oct. 2016, pp. 1–4.

[7] Z. Zhang, H. Zhao, J. Wang, and Y. Shen, "Signal-multiplexing ranging for network localization," *IEEE Trans. Wireless Commun.*, vol. 21, no. 3, pp. 1694–1709, Mar. 2022.

[8] H. Zhao, Z. Zhang, L. Xu, Y. Wang, and Y. Shen, "Enhancing timeliness in asynchronous vehicle localization: A signal-multiplexing network measuring approach," *IEEE Transactions on Intelligent Transportation Systems*, pp. 1–15, 2024.

[9] A. Goudar, F. Dümbgen, T. D. Barfoot, and A. P. Schoellig, "Optimal initialization strategies for range-only trajectory estimation," *IEEE Robotics and Automation Letters*, vol. 9, no. 3, pp. 2160–2167, 2024.

[10] A. Ledergerber, M. Hamer, and R. D'Andrea, "Angle of arrival estimation based on channel impulse response measurements," in *2019 IEEE/RSJ International Conference on Intelligent Robots and Systems (IROS)*, 2019, pp. 6686–6692.

[11] I. Dotlic, A. Connell, H. Ma, J. Clancy, and M. McLaughlin, "Angle of arrival estimation using DecaWave DW1000 integrated circuits," in *Proc. Workshop Pos., Nav. Commun.*, Bremen, Germany, Oct. 2017, pp. 1–6.

[12] E. Kornaros, S. Kabiri, and F. De Flaviis, "A novel model for direction finding and phase center with practical considerations," *IEEE Trans. Antennas Propag.*, vol. 65, no. 10, pp. 5475–5491, Oct. 2017.

[13] Z.-M. Liu, C. Zhang, and P. S. Yu, "Direction-of-arrival estimation based on deep neural networks with robustness to array imperfections," *IEEE Trans. Antennas Propag.*, vol. 66, no. 12, pp. 7315–7327, Dec. 2018.

[14] F. Ge and Y. Shen, "Single-anchor ultra-wideband localization system using wrapped pdoa," *IEEE Trans. Mobile Comput.*, vol. 21, no. 12, pp. 4609–4623, Dec. 2022.

[15] T. Liu, B. Li, and L. Yang, "Phase center offset calibration and multipoint time latency determination for UWB location," *IEEE Internet Things J.*, vol. 9, no. 18, pp. 17 536–17 550, Sep. 2022.

[16] M. Wax and R. Tweg, "Direction of arrival tracking below the ambiguity threshold," *IEEE Trans. Aerosp. Electron. Syst.*, vol. 36, no. 2, pp. 354–363, Apr. 2000.

[17] H. Chen, T. Ballal, N. Saeed, M.-S. Alouini, and T. Y. Al-Naffouri, "A joint TDOA-PDOA localization approach using particle swarm optimization," *IEEE Wireless Commun. Lett.*, vol. 9, no. 8, pp. 1240–1244, Aug. 2020.

[18] P. Steigenberger, M. Fritsche, R. Dach, R. Schmid, O. Montenbruck, M. Uhlemann, and L. Prange, "Estimation of satellite antenna phase center offsets for galileo," *J. Geod.*, vol. 90, pp. 773–785, May 2016.

[19] M. Titsias, "Variational learning of inducing variables in sparse gaussian processes," in *Proc. Int. Conf. Artif. Intell. Stat.*, vol. 5, Clearwater Beach, Florida, Apr. 2009, pp. 567–574.

[20] LUSTER LightTech Co., Ltd., "FZMotion Mocap System." [Online]. Available: https://www.luster3ds.com